Akshay Kale[1]
Saurin Patel[1]
Guoqing Hu[2]*
Xiangchun Xuan[1]

[1]Department of Mechanical Engineering, Clemson University, Clemson, SC, USA
[2]LNM, Institute of Mechanics, Chinese Academy of Sciences, Beijing, P.R. China

Received September 14, 2012
Revised October 29, 2012
Accepted October 30, 2012

Research Article

Numerical modeling of Joule heating effects in insulator-based dielectrophoresis microdevices

Insulator-based DEP (iDEP) has been established as a powerful tool for manipulating particles in microfluidic devices. However, Joule heating may become an issue in iDEP microdevices due to the local amplification of electric field around the insulators. This results in an electrothermal force that can manifest itself in the flow field in the form of circulations, thus affecting the particle motion. We develop herein a transient, 3D, full-scale numerical model to study Joule heating and its effects on the coupled transport of charge, heat, and fluid in an iDEP device with a rectangular constriction microchannel. This model is validated by comparing the simulation results with the experimentally obtained fluid flow patterns and particle images that were reported in our recent works. It identifies a significant difference in the time scales of the electric, temperature, and flow fields in iDEP microdevices. It also predicts the locations of electrothermal flow circulations in different halves of the channel at the upstream and downstream of the constriction.

Keywords:
Electrokinetic / EOF / Electrothermal flow / Insulator-based dielectrophoresis / Joule heating / Microfluidics
DOI 10.1002/elps.201200501

Additional supporting information may be found in the online version of this article at the publisher's web-site

1 Introduction

Insulator-based DEP (iDEP) has been established as a powerful tool for manipulating particles in microfluidic devices [1–17]. However, the local amplification of electric fields around the in-channel insulators makes iDEP microdevices susceptible to Joule heating [18, 19], which can cause adverse effects to both the treated samples and the devices [20]. So far Joule heating and its effects have been extensively studied in electrophoresis and electrode-based pumping/dielectrophoresis devices [21–25], but the study of this topic in iDEP microdevices are still significantly lacking.

Recently, Hawkins et al. [26] predicted in a 2D numerical model the existence of electrothermal flow circulations near the depth-wise channel constriction of an iDEP device. They also carried out a parametric study and found that electrothermal flow effects enhance the dielectrophoretic particle deflection in their device [26]. A recent work from our group [27] experimentally verified the prediction of electrothermal flow circulations in a rectangular microchannel with a widthwise constriction. Moreover, a 2D numerical model was developed to simulate the Joule heating effects on EOF through the same channel, and a good agreement was achieved for the observed flow pattern. However, the model considered only the fluid domain and must assume an unrealistically large convective heat transfer coefficient [27]. More recently our group [28] experimentally demonstrated that Joule heating reduces the electrokinetic focusing and trapping of particles in widthwise constriction microchannels by the use of two different channel depths. However, a quantitative understanding of the effects of Joule heating on particle motion is yet to be developed.

This work demonstrates for the first time a transient, 3D, full-scale numerical modeling of Joule heating and its effects on electrokinetic fluid flow and particle motion in iDEP microdevices. The transient development of the coupled electric, temperature, and flow fields is investigated. The effects of electric field, geometric parameters of the microchannel,

Correspondence: Professor Xiangchun Xuan, Department of Mechanical Engineering, Clemson University, Clemson, SC 29634-0921, USA
E-mail: xcxuan@clemson.edu
Fax: +1-864-656-7299

Abbreviation: iDEP, insulator-based DEP

*Additional corresponding author: Guoqing Hu,
E-mail: guoqing. hu@imech.ac.cn

Colour Online: See the article online to view Figs. 1–8 in colour.

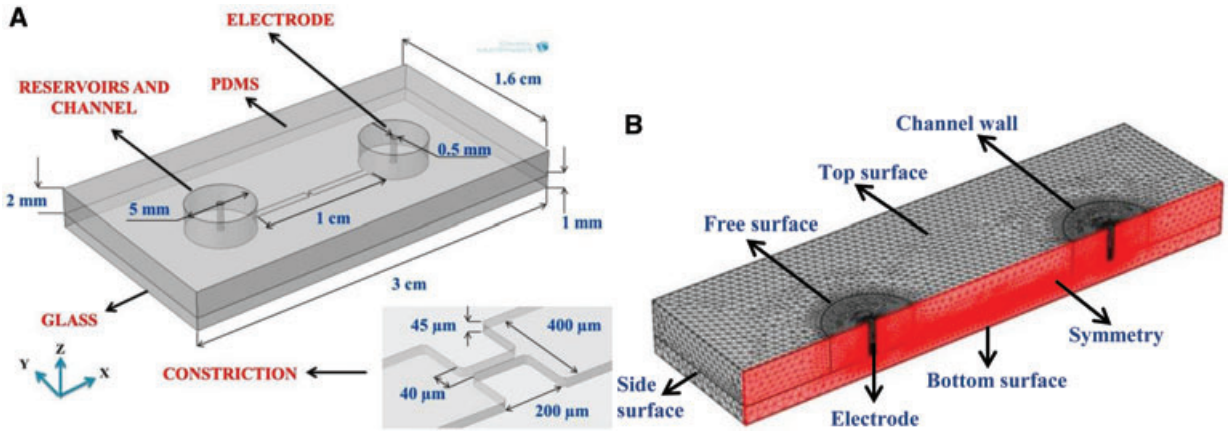

Figure 1. (A) Isometric view of the experimentally used iDEP device with dimensions indicated (the inset shows a close-up view of the microchannel constriction). (B) Meshed computational domain with labeled surface boundaries (the symmetry plane is highlighted).

and electric properties of the fluid are investigated on the steady-state fluid temperature and flow fields. The numerical predictions are compared with the experimental results reported in our recent works [27, 28].

2 Theory

2.1 Computational domain

This work extends the 2D steady-state model developed in our recent work [27] to 3D and transient. The computational geometry considers the full-scale microfluidic device used in the experiments [27, 28], which covers the fluid in the microchannel and inlet/outlet reservoirs, the PDMS and glass substrates, and the platinum electrodes in the inlet/outlet reservoirs. Figure 1A shows an isometric view of the computational geometry (to scale) with the dimensions of each component being labeled. Since the physics observes a symmetric behavior about the longitudinal center-plane of the microchannel, only half of this geometry is used in our numerical model. Figure 1B illustrates the meshed computational domain, on which the surfaces to be imposed with boundary conditions have been labeled. The origin of this 3D model is taken at the center of the channel-glass interface. Hence the PDMS and glass substrates lie in the positive and negative portions of the z-axis, respectively. The electrodes are assumed to extend in the fluid vertically down to half the depth of the channel from the center of the reservoir free surface. As their thermal and electric conductivities are high enough to maintain a uniform temperature and voltage, the electrodes are simply treated as holes with given surface conditions in the model.

2.2 Transport equations with initial and boundary conditions

The following sections present the transport equations for charge, heat, fluid, and particles that are involved in the process of iDEP device operation. Also presented are the initial and boundary conditions on the surfaces indicated in Fig. 1B for each of these equations. Note that due to the temperature-dependent fluid properties, especially the dynamic viscosity η, electric conductivity σ, and permittivity ε, the transport equations of charge, heat, and fluid are coupled and must be solved simultaneously in the numerical model.

2.2.1 Transport of charge: electric field

The transient electric field, E, in a moving electrolyte is governed by the current conservation equation. For absence of any external sources of charge and current, and assuming that the convective current is insignificant, the equation can be expressed as [26, 27, 29]:

$$\nabla \cdot \left(\sigma \mathrm{E} + \frac{\partial \mathrm{D}}{\partial \mathrm{t}}\right) = 0 \text{ and } \mathrm{E} = -\nabla\phi \tag{1}$$

where $\mathrm{D} = \varepsilon\,\mathrm{E}$ is the electric field displacement, t is the time coordinate, and ϕ is the electric potential. It is important to note here that since we are dealing with a DC-biased AC voltage, as in the experiments discussed previously [27, 28], the transient variation of the electric displacement occurs due to two factors. They are the frequency of the AC component of the electric field and the variation of the electric field over the observation time due to the change in the temperature field. However, the frequency of the AC field in the experiments [27, 28] is fixed at 1 kHz and much smaller than the charge relaxation frequency $\sigma/(2\pi\varepsilon)$ [23, 24] (in the order of 10 MHz). Hence the frequency effects on the electric displacement are negligible and its variation with time can be considered solely due to the variation of temperature. The electric field is restricted only to the fluid domain by electrically insulating the channel walls. The two electrodes are imposed with the experimentally applied voltage and zero voltage (i.e. grounded), respectively. The initial value of the electric potential is zero everywhere within the fluid.

2.2.2 Transport of heat: temperature field

The electric field established in the microchannel leads to Joule heating in the electrolyte, which is very high in the constriction region due to the locally amplified electric field. This generated heat gives rise to temperature gradients that spreads across the fluid, PDMS, and glass with time. The temperature field, T, over the entire device is governed by the energy equation:

$$\rho C_p \left(\frac{\partial T}{\partial t} + U \cdot \nabla T \right) = k \nabla^2 T + \sigma E^2 \tag{2}$$

where ρ, C_p, and k are the mass density, heat capacity, and thermal conductivity of either the fluid or the solid substrate, and **U** is the fluid velocity. The last term on the right-hand-side of Eq. (2) represents the volumetric Joule heat generation, which exists only in the fluid domain. This heat is transferred through convection and conduction in the fluid and pure conduction across the PDMS and glass substrates. It is eventually dissipated to air through convection from the top (PDMS), side (PDMS and glass), and bottom (glass) surfaces of the device as indicated in Fig. 1B. Appropriate correlations are used for computing the heat transfer coefficients at each of these convective surfaces, the details of which are given in the Supporting Information. The Free surface of the fluid [see Fig. 1B] in the reservoir is assumed to obey the same correlation as that of the Top surface of the PDMS. The platinum Electrodes are assumed to be isothermal at room temperature. The initial temperature of the whole device is set to room temperature.

2.2.3 Transport of fluid: flow field

The flow field in the fluid is governed by the continuity equation and the incompressible Navier–Stokes equations [27,29]:

$$\nabla \cdot U = 0 \tag{3}$$

$$\rho \left(\frac{\partial U}{\partial t} + (U \cdot \nabla) U \right) = -\nabla p + \nabla \cdot (\eta \nabla U) + \nabla \cdot (\varepsilon E) E - \frac{1}{2} (E \cdot E) \nabla \varepsilon \tag{4}$$

where p is the hydrodynamic pressure. The last two terms on the right-hand-side of Eq. (4) are the Coulomb forces on free and bound charges, respectively [26,29,30]. The combination of these two electric body forces can be called the electrothermal force here as the involving permittivity gradient, $\nabla\varepsilon$, is caused by Joule heating-induced temperature gradient, ∇T. The transformation from $\nabla\varepsilon$ to ∇T in terms of the temperature dependence of ε has been discussed in previous works [26,27] and is thus skipped here. As the electric double layer (on the order of few nanometers) is very thin compared to the microchannel dimensions, the well-accepted electroosmotic slip velocity, $u = (-\varepsilon\zeta/\eta)E_{DC}$ with ζ being the wall zeta potential and E_{DC} the DC component of the electric field, can be applied to the channel wall (including the walls of the microchannel and reservoirs) (see Fig. 1B). The Free surfaces of the fluid in the inlet and outlet reservoirs are assumed to be exposed to atmosphere. The entire fluid is assumed still initially.

2.2.4 Transport of particles: trajectory

The trajectory of a particle in the fluid is determined by its velocity relative to the channel wall, U_p, which is given by the vector sum of the fluid velocity, electrophoretic velocity of the particle if charged, U_{EP}, and dielectrophoretic velocity of the particle regardless of its charge, U_{DEP}, i.e.

$$U_P = U + U_{EP} + U_{DEP} \tag{5}$$

$$U_{EP} = -\frac{\varepsilon \zeta_P}{\eta} E_{DC} \tag{6}$$

$$U_{DEP} = \lambda \frac{d^2 \varepsilon}{12\eta} f_{CM} \nabla \left(E_{DC}^2 + E_{AC}^2 \right) \tag{7}$$

where ζ_p is the particle zeta potential, λ is the correction factor that we introduce to account for the effects of particle size on dielectrophoretic velocity and has been proved reasonable in previous 2D simulations [7, 11, 15, 17, 19], d is the particle diameter, f_{CM} is the Clausius–Mossotti factor [31] that is a function of the electric conductivities of the fluid and particle at DC and low-frequency AC electric fields (typically $<$ 100 kHz) [1–4, 20], and E_{AC} the AC component of the electric field that does not contribute to particle electrophoresis.

2.3 Numerical method and material properties

COMSOL Multiphysics 4.2a (COMSOL), a commercial finite element simulation software, was used to generate the 3D numerical model. The "electric currents" and "conjugate heat transfer" interfaces in the software were coupled together for solving the above transport equations. The previous approach [27] of solving for all the fields under the influence of the DC component of the applied voltage, and including the influence of the AC component by defining an AC to DC voltage ratio was repeated for the current modeling. The expressions for the current conservation in Eq. (1), heat source in Eq. (2), electric body force in Eq. (4), and the dielectrophoretic velocity in Eq. (7) are modified accordingly, the details of which are presented in the Supporting Information. The constriction region of the microchannel was meshed extremely finely compared to the remaining part for accommodating the local high field gradients [see Fig. 1B]. This required a total of about 1.5 million elements to obtain a grid-independent solution. A nonlinear, segregated, iterative solver was used in the modeling for minimizing the computational memory and time. Appropriate damping factors were employed to establish a faster convergence. Considering the memory intensive requirements for obtaining grid-independent solutions, the generated case files were solved in the Palmetto

Cluster, an efficient high performance computing facility of Clemson University. The obtained solutions were postprocessed in COMSOL and exported in the form of data or images. "Particle Tracing" module in COMSOL was employed to simulate the particle trajectory using the particle velocity in Eq. (5). Considering the electric conductivity of the fluid is much larger than that of the particle, we simply set the Clausius–Mossotti factor, f_{CM}, in Eq. (7) to −0.5.

The coupled effects of Joule heating on the above-presented transport fields are addressed by the use of the following expressions for temperature dependent fluid properties [21, 27]:

$$\sigma = \sigma_0[1 + \alpha\,(T - T_0)] \tag{8}$$

$$\varepsilon = \varepsilon_0[1 + \alpha\,(T - T_0)] \tag{9}$$

$$\eta = 2.761 \times 10^{-6}\exp(1713/T) \tag{10}$$

where the subscript 0 indicates the value of the corresponding property at the room temperature, T_0, and α and β are the temperature coefficients of electric conductivity and permittivity, respectively. The values of the constants and material properties involved in the numerical simulation are listed in Table 1 [27] (http://www.mit.edu/~6.777/matprops/pdms.htm; Material Library, COMSOL Multiphysics 4.2a, COMSOL Inc., Burlington, MA). Note that we did not consider the temperature dependence of wall and particle zeta potentials in the model [32]. The wall zeta potential value was obtained from [33]. The particle zeta potential value was estimated from the measured electrokinetic particle velocity (a combination of fluid electroosmosis and particle electrophoresis) under a small DC voltage, at which Joule heating effects are negligible [21].

Table 1. Summary of the constants and material properties used in the model

Symbol	Value	Unit	Description
T_0	293	K	Room temperature
σ_0	0.047	S/m	Fluid electric conductivity at T_0
α	0.02	1/K	Temperature coefficient of fluid electric conductivity
ε_0	$7.10E^{-10}$	F/m	Fluid permittivity at T_0
β	−0.0046	1/K	Temperature coefficient of permittivity
ρ	1000	kg/m^3	Fluid density
C_p	4.186	kJ/(kg·K)	Fluid heat capacity
k	0.6	W/(m·K)	Fluid thermal conductivity
ζ	−50	mV	Wall zeta potential
ρ_{PDMS}	970	kg/m^3	PDMS density
$C_{p(PDMS)}$	1.46	kJ/(kg·K)	PDMS heat capacity
k_{PDMS}	0.15	W/(m·K)	PDMS thermal conductivity
ρ_{glass}	2203	kg/m^3	Glass density
$C_{p(glass)}$	0.703	kJ/(kg·K)	Glass heat capacity
k_{glass}	1.38	W/(m·K)	Glass thermal conductivity
ζ_P	−35	mV	Particle zeta potential
λ	0.8	—	Correction factor for dielectrophoretic velocity
f_{CM}	−0.5	—	Clausius–Mossotti factor
d	3	μm	Particle diameter

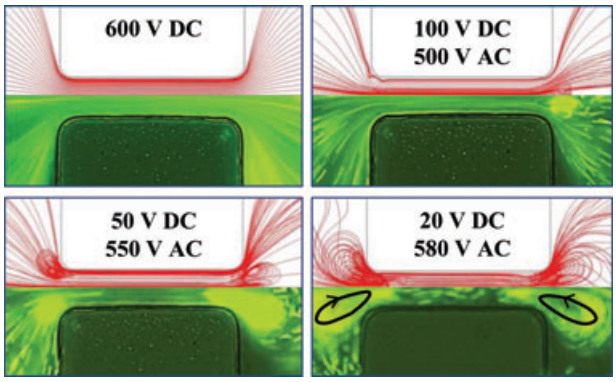

Figure 2. Comparison of the numerically predicted fluid streamlines from the 3D model (top) and the experimentally obtained particle streak images (bottom, the experimental detail is referred to [27]) in the microchannel constriction region of an iDEP device under various DC-biased AC (fixed at 1 kHz) voltages. The average electric field is 600 V/cm over the channel length in all four cases where the flow direction is from left to right. The arrowed loops in the experimental image of the 20V DC / 580 V AC case indicates the directions of the electrothermal flow circulations.

2.4 Model validation

To validate the above-described 3D transient model, we performed numerical simulations for the experimental cases reported in our recent work on Joule heating effects in an iDEP device identical to that in Fig. 1A [27]. The steady-state numerical results are compared with the DC-biased AC voltage driven experiments in terms of the obviously visible phenomenon, i.e. the fluid flow circulations generated at the necks of the constriction by the electrothermal force in Eq. (4) (see the last two terms). Figure 2 shows the case-to-case comparison between the numerically predicted fluid streamlines (top image in each panel) and the experimentally recorded streak images of 590 nm green fluorescent polystyrene particles (bottom image in each panel). The 3D numerical model is seen to simulate the experiment with a good agreement for all the four cases as illustrated in Fig. 2. This model is therefore validated as a good model for investigating the effects of Joule heating on electrokinetic fluid and particle motions in iDEP devices, which will be presented in the results section below.

3 Results and discussion

3.1 Transient development of transport fields

This section investigates the transient development of the coupled electric, temperature, and flow fields in iDEP

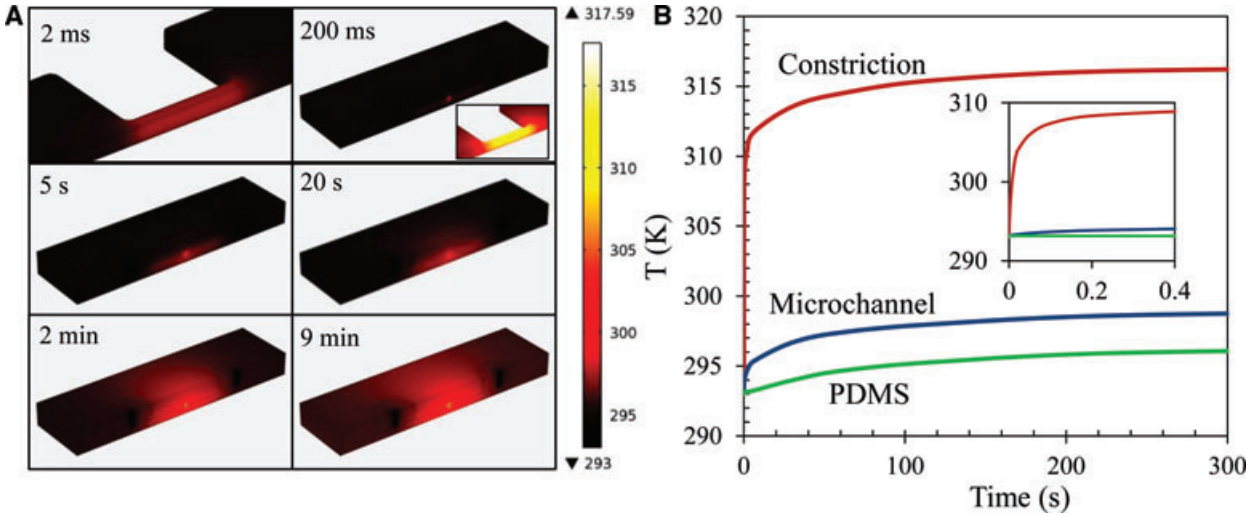

Figure 3. (A) Transient development of the temperature field in the iDEP device over a time period of 9 min. The top-left image displays the temperature field only in the constriction region, which is also the case for inset of the top-right image. (B) Temperature-time curves at three locations of the device: center point of the channel constriction (labeled as constriction), center point of the channel section on the upstream side of the constriction (labeled as microchannel), and center point of the PDMS domain (labeled as PDMS). The inset of (B) shows a close-up view of the T-t curves in the initial 0.4 s.

microdevices. Only DC-biased AC voltages are considered here due to the recently increasing use of AC/DC electrokinetic flow in iDEP microdevices [9–11, 15–17, 26–28]. This is because AC voltages contribute to particle DEP while not affecting electrokinetic transport and so the introduction of AC voltages can greatly enhance the flexibility in particle control. A reference case of 50 V DC/550 V AC is used for the demonstration. All other conditions are referred to Table 1. The dimensions of the simulated iDEP device are referred to Fig. 1A.

3.1.1 Temperature field

Figure 3A shows the transient development of the temperature field over the entire system. The electric field is established virtually immediately, so is Joule heating, and hence the constriction region is seen to heat up within 2 ms. The heat then propagates outside the constriction as time elapses. In about 200 ms, the spatial temperature field in the fluid is completely developed throughout the microchannel. The further change in the fluid temperature field is similar everywhere, i.e. simply an increase in magnitude as time progresses. The temperature profile in the constriction shifts towards the downstream region owing to the fluid flow, which has been also predicted in previous 2D model [26, 27]. After 5 s, the heat propagates along the entire depth of the glass domain below the constriction and begins to diffuse laterally thereafter. The PDMS region follows the same trend, but its lower thermal diffusivity increases the thermal diffusion time. It takes about 20 s for heat to begin diffusing laterally in PDMS. Still the lateral diffusion of heat is very slow in both domains. The regions of and beyond the reservoir begin to heat up after about 2 min, but the temperature rise thereafter is no more than 2 K due to its large distance from the constriction. The system temperature reaches a steady state in about 8–9 min.

Figure 3B shows the temperature-time (T-t) graphs at three different locations, which are the center points of the channel constriction, the channel section on the upstream side of the constriction, and the PDMS domain, respectively. The T-t graph for the last location is noticed to almost overlap with that at the center point of the glass domain (data not shown). All these curves follow a similar trend, with an initially high rate of temperature rise, and then a gradual one. When the spatial development of the temperature field over the entire device is complete, the distribution thereafter simply increases in magnitude. This is illustrated by the parallel nature of the T-t curves after about 2 min. However, the initial temperature increase rates are significantly different at the three illustrated locations in Fig. 3B. The fluid experiences the initial influence of Joule heating in a much quick way than the glass and PDMS substrates. This happens because Joule heating is confined within the fluid. Moreover, the fluid temperature in the constriction center has a significantly larger initial rate of increase than that away from the constriction, which is evidenced from the inset of Fig. 3B.

3.1.2 Electric field

As noted earlier, the transient development of electric field is coupled with that of the temperature field in the fluid domain, between which, however, the former develops much faster.

This is evidenced in Fig. 4A by the electric field profiles along the center line of the microchannel at different time instants ranging from 0 s to 200 ms. Beyond 200 ms, the electric field profile remains nearly unvaried and is not shown in

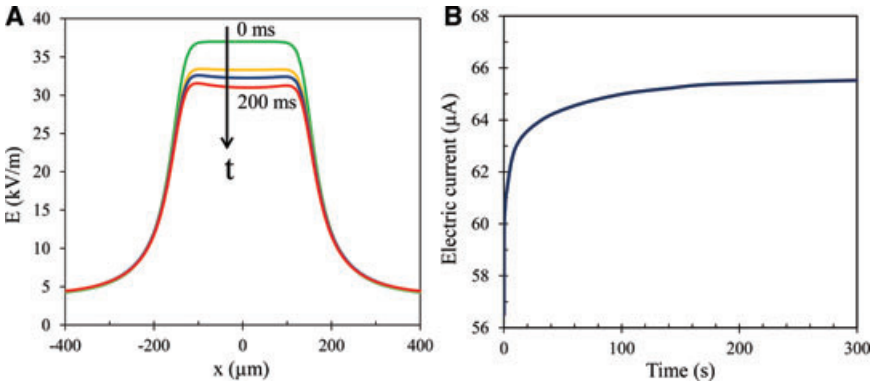

Figure 4. (A) Transient development of electric field along the channel centerline in the range of 800 μm about the constriction (i.e. $x = 0$). The arrow indicates the direction of time increase, which starts from 0 s to 10 ms, 20 ms, and ends at 200 ms corresponding to the four electric field profiles. (B) Electric current-time graph for the first 5 min.

the figure. One can see that the electric field is established virtually immediately in the fluid, i.e. at $t = 0$ ms. Although this is theoretically impossible, the infinitesimally small time scale for electric field generation is good enough for us to assume so. As time goes on, the electric field magnitude in the constriction decreases. This is in accordance with the current conservation law and the increase of electric conductivity with temperature. Also, with the passage of time the rate of rise in temperature decreases (see Fig. 3), so does the rate of drop in the electric field magnitude in the constriction region. In contrast, the electric field in the region away from the constriction can be said to maintain a steady-state throughout, owing to its much smaller magnitude than that in the constriction and as well a much lower rate of rise of the local fluid temperature. Within 200 ms the temperature profile in the fluid becomes almost fully developed and the rate of temperature rise thereafter is small enough to maintain the electric field at steady state.

Figure 4B shows the electric current-time graph. Due to the infinitesimally small time scale for electric field development, the generation of current through the fluid is an impulse response. Thus, initially, a current of about 56 μA is set up in the channel, which can be viewed as the current in the absence of Joule heating effects. This current initially rises fast to reach about 66 μA in a time span of 2 min. This prediction agrees well with the experimental observation described in the previous work [27]. The further rise in the current is very slow and after about 5 min the current almost maintains itself at a steady value. This entire trend can be attributed to the initially sharp and later a gradual rise in the electric conductivity as a consequence of the fluid temperature development in Fig. 3B.

3.1.3 Flow field

The flow field is a superposition of the DC EOF that originates from the slip velocity on the channel walls and the AC/DC electrothermal flow that is generated by the electrothermal force (see the last two terms in Eq. (4)). Hence, its transient development can also be understood from that of each of these two flows. Figure 5A shows the transient development of fluid streamlines in the constriction region. One can see that the EOF develops as soon as the electric field is initiated and acts in the direction of the applied electric field. In the first 2 ms, the electrothermal flow is not strong enough to disrupt the EOF and so the fluid streamlines are still aligned along the length of the channel. After that Joule heating begins to manifest its effects on fluid electroosmosis in the form of electrothermal circulations. Hence the fluid streamlines no longer align themselves with the direction of the electric field, and begin to bend inwards at each neck.

Interestingly, the downstream circulation initiates closer to the bottom of the channel and the upstream one closer to the top of the channel, which has not been reported previously. This phenomenon can be explained using the electrothermal force in Eq. (4), which is mainly governed by the last term scaling with the reverse of the permittivity gradient and hence the temperature gradient (note that the permittivity gradient is in a direction opposite to the temperature gradient). Such a dielectric force thus assumes a negative and a positive value at the downstream and upstream of the constriction, respectively, due to the local negative and positive temperature gradients. Therefore the local values of electrothermal force are larger for lower temperature gradients in the downstream region, i.e. closer to the bottom half, and smaller for higher temperature gradients in the upstream region, i.e. closer to the top half. In addition, the downstream circulation is found larger than the upstream one because the convection shifts the high temperature zone toward the downstream neck of the constriction. The circulations grow in size continuously with time and become significantly large in about 10 ms. Meanwhile the temperature gradients about the constriction also start to get spatially developed. Hence the fluid circulations grow comparatively at a smaller rate from 10 ms onwards.

Figure 5B shows the fluid volume flow rate-time graph through the constriction microchannel. As Joule heating develops almost instantly in the constriction region (see Fig. 3), there exists an initial sharp increase in the flow rate due to the change in fluid properties. However, with the quick development of electrothermal flow (circulations), the flow rate starts to drop from about 2 ms through 50 ms. Thereafter, although the temperature and electric fields are still under development, they are high enough for their gradients to

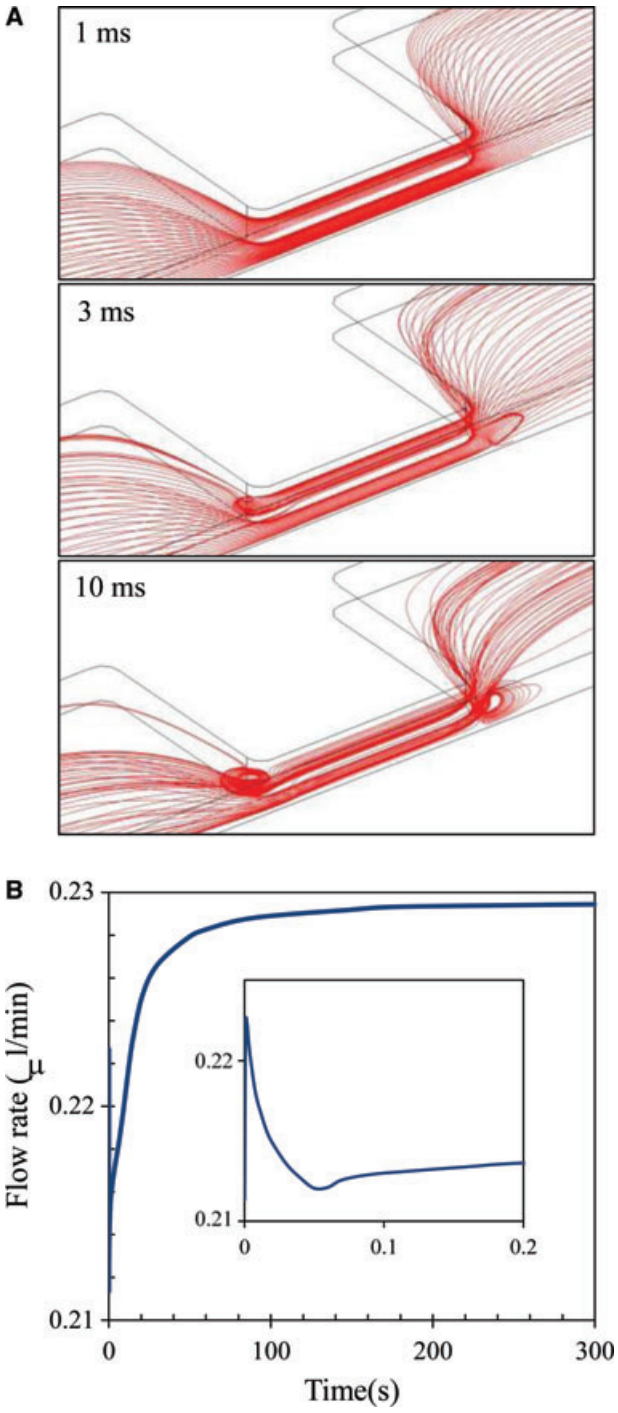

Figure 5. (A) Transient development of fluid streamlines in the channel constriction region of an iDEP device. (B) Volume flow rate-time graph with the inset being a close-up view in the initial 0.2 s.

exhibit a very small change with time in the constriction region, and hence the electrothermal flow can be assumed to attain a steady state in 50 ms. The further rise in the flow rate after 50 ms is a result of the increase in the electroosmotic slip velocity due to temperature increase, which is evidenced

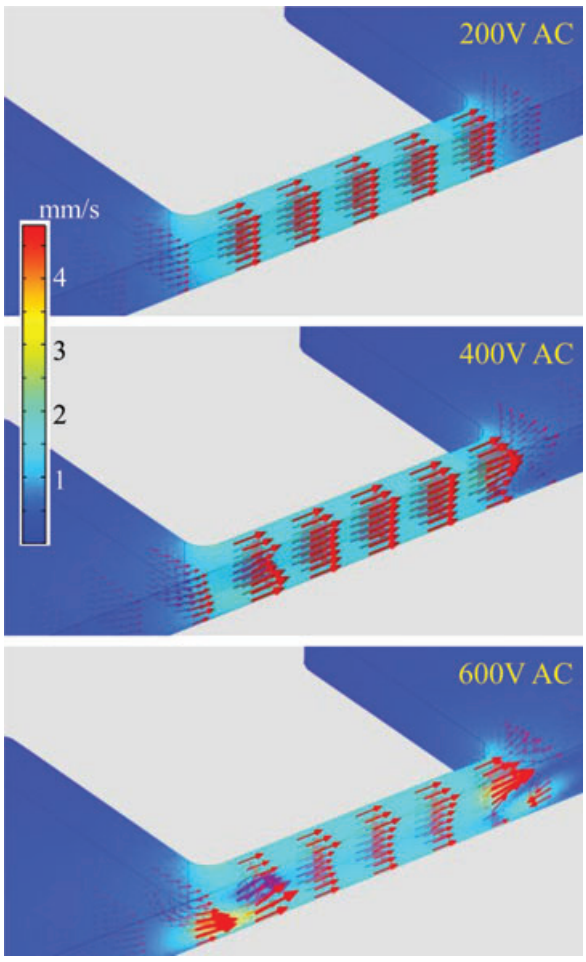

Figure 6. Fluid velocity vectors and magnitude across the microchannel constriction for different values of AC voltages. The DC voltage is fixed at 50 V.

by the similar time graphs between flow rate in Fig. 5B and fluid temperature in Fig. 3B.

3.2 Parametric effects on steady-state transport fields

This section examines the parametric effects on the steady-state solutions of temperature, electric, and flow fields in iDEP microdevices. Joule heating effects on electrokinetic particle transport in iDEP devices are studied in the next section.

3.2.1 Effects of AC to DC voltage ratio

To study the effects of AC to DC voltage ratio, we fix the DC voltage at 50 V while varying the AC voltage from 200 V to 400 V and 600 V. The rise in the fluid temperature is expected because a larger AC component increases Joule heating. The AC voltage also affects the flow field due to the fact that it

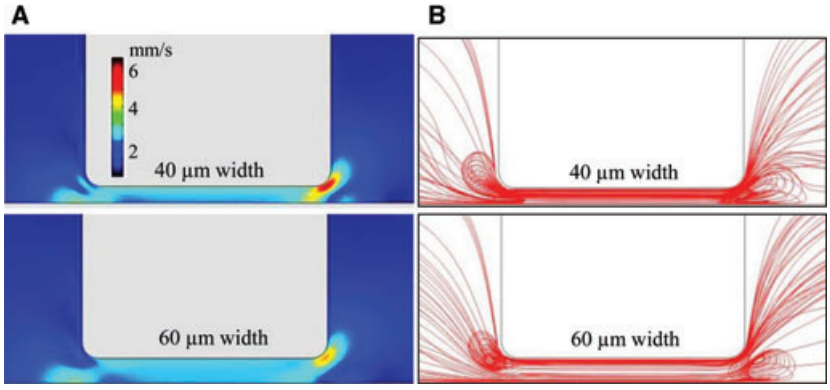

Figure 7. Effect of constriction width on fluid velocity magnitude (A) and fluid streamlines (B) in 40 μm and 60 μm wide constrictions under 50 V DC/550 V AC. All other conditions remain the same between the two cases and are referred to Table 1 and Fig. 1A.

alters the temperature and electric field gradients and hence the electrothermal force. Such influences increase at a higher AC voltage as seen from the fluid velocity vectors in Fig. 6. Specifically the electrothermal force at 200 V AC is not strong enough to influence the EOF field. At 400 V AC, however, the velocity vectors tend to turn around at the downstream neck of the constriction, thereby indicating the growth of a minute flow circulation. At 600 V AC, the electrothermal force becomes so strong that flow circulations are formed at both sides of the constriction.

3.2.2 Effects of constriction width

The constriction width is an important geometrical parameter that determines the electric field gradients and hence the dielectrophoretic force in iDEP devices. Figure 7 compares the fluid velocity magnitude (A) and streamlines (B) in 40 μm and 60 μm wide constrictions with all the other parameters being kept identical. In a narrower constriction, the electric field amplification increases by 50% and so Joule heating is about 125% higher. However, the enhanced EOF extracts more heat away from the narrower constriction. These combined effects lead to a 4 K rise in the fluid temperature in the 40 μm wide constriction compared to the 60 μm one. The consequence of the amplified electric field and the fluid temperature rise is an enhanced electrothermal flow circulation in both strength and size as demonstrated in Fig. 7.

3.2.3 Effects of other parameters

We have also used the 3D numerical model to study the effects of the length and corner radius of the constriction and the electric conductivity of the fluid on the transport fields in iDEP devices. The results are presented in the Supporting Information.

3.3 Joule heating effects on electrokinetic particle transport

In this section we use the 3D numerical model to simulate and understand the experimentally observed Joule heating effects on electrokinetic particle transport that was reported in our recent work [28]. Two depths of constriction microchannels were used in the experiment, which are 45 μm and 15 μm, respectively. The former is identical to the reference channel used in the transient state study discussed above (see Section 3.1). Figure 8 compares the numerically predicted trajectories

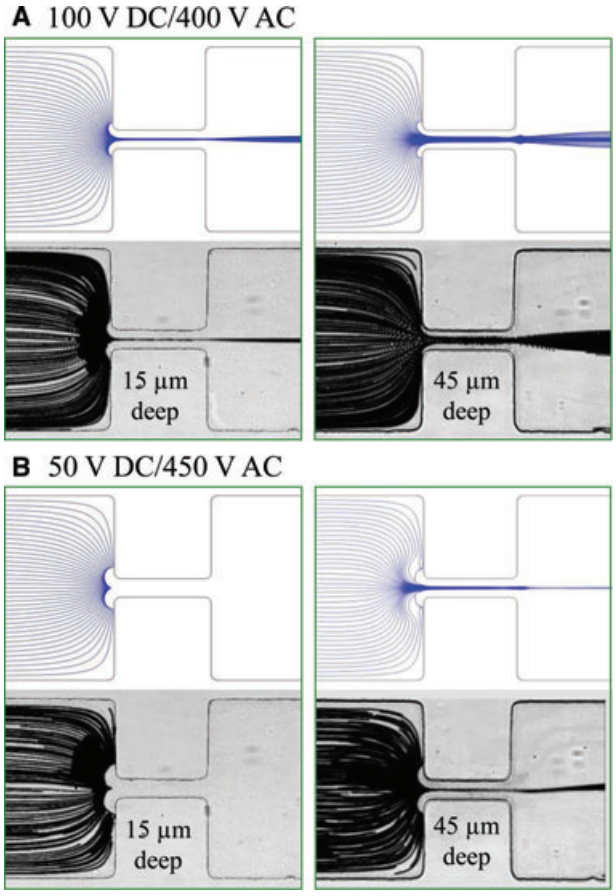

Figure 8. Comparison of the numerically predicted trajectories (top image in each panel) and experimentally obtained streak images (bottom image in each panel, copied from [28] with permission) of 3 μm polystyrene particles in 15 μm (left column) and 45 μm deep constriction microchannels (right column) under 100 V DC/400 V AC (A) and 50 V DC/450 AC (B).

and experimentally recorded streak images of 3 μm particles in the two depths of microchannels under 100 V DC/400 V AC (A) and 50 V DC/450 AC (B), respectively. Note that steady-state temperature, electric, and flow fields are assumed in the simulation. A close agreement is seen between modeling and experimental results in all cases. Specifically, particles are focused toward the center of the channel by iDEP, which increases at a larger AC to DC voltage ratio and is applicable to both depths of channels. However, the extent of focusing is always stronger in the 15 μm deep channel than in the 45 μm one, especially significant in the 50 V DC/450 V AC case where particles can be trapped in the shallower channel while not in the other. These discrepancies can be attributed to the impact from Joule heating in two aspects: one is the reduced electric field gradient at a higher fluid temperature, which can be referred to Fig. 3A and is a consequence of the electric current conservation. The mathematical explanation for this is provided in the Supporting Information. The other reason lies in the Joule heating enhanced electroosmotic and electrothermal flows, especially the latter because of the flow circulations as demonstrated in Fig. 6.

4 Concluding remarks

We have developed a transient 3D numerical model to study Joule heating and its effects on electrokinetic fluid flow and particle motion in iDEP microdevices. This model has been validated by comparing the numerical predictions with the experimentally observed fluid streamlines and particle trajectories that were reported in our recent works [27, 28]. It establishes for the first time a significant difference in the time scales of the temperature, electric and flow fields in iDEP devices. It also predicts the formation of electrothermal flow circulations in different halves of the microchannel at the two sides of the constriction, which has not been reported in previous 2D numerical models [26, 27] and certainly warrants a further study. Such circulations may potentially be used to facilitate the trapping of biomolecules (e.g. DNA and protein) that are too small to be efficiently handled in iDEP microdevices [34]. The parametric study we have done in this work can support this motive by helping enhancing the efficiency of this manipulation based on the size and strength of the flow circulations.

This work is supported by NSF under grant CBET-0853873 and by Clemson University through the University Research Grant (X. Xuan). The support from MOST (2011CB707604), NSFC (11272321, 11102214), and CAS (KJCX2-YW-H18) to G. Hu is gratefully appreciated as well. We also acknowledge the Open Fund support from LNM.

The authors have declared no conflict of interest.

5 References

[1] Hawkins, B. G., Gleghorn, J. P., Kirby, B. J., in: Zahn, J. D. (Ed.), *Methods in Bioengineering: Biomicrofabrication and Biomicrofluidics*, Artech Press, Cedar Knolls, NJ, 2009, pp. 133–181.

[2] Srivastava, S. K., Gencoglu, A., Minerick, A. R., *Anal. Bioanal. Chem.* 2010, *399*, 301–321.

[3] Regtmeier, J., Eichhorn, R., Viefhues, M., Bogunovic, L., Anselmetti, D., *Electrophoresis* 2011, *32*, 2253–2273.

[4] Cetin, B., Li, D., *Electrophoresis* 2011, *32*, 2420–2427.

[5] Lapizco-Encinas, B. H., Simmons, B. A., Cummings, E. B., Fintschenko, Y., *Electrophoresis* 2004, *25*, 1695–1704.

[6] Barrett, L. M., Skulan, A. J., Singh, A. K., Cummings, E. B., Fiechtner, G. J., *Anal. Chem.* 2005, *77*, 6798–6804.

[7] Kang, K. H., Kang, Y., Xuan, X., Li, D., *Electrophoresis* 2006, *27*, 694–702.

[8] Pysher, M. D., Hayes, M. A., *Anal. Chem.* 2007, *79*, 4552–4557.

[9] Hawkins, B. G., Smith, A. E., Syed, Y. A., Kirby, B. J., *Anal. Chem.* 2007, *79*, 7291–7300.

[10] Lewpiriyawong, N., Yang, C., Lam, Y. C., *Biomicrofluid* 2008, *2*, 034105.

[11] Zhu, J., Xuan, X., *Electrophoresis* 2009, *30*, 2668–2675.

[12] Ai, Y., Qian, S., Liu, S., Joo, S. W., *Biomicrofluid* 2010, *4*, 013201.

[13] Baylon-Cardiel, J. L., Jesus-Perez, N. M., Chavez-Santoscoy, A. V., Lapizco-Encinas, B. H., *Lab. Chip.* 2010, *10*, 3235–3242.

[14] Gallo-Villanueva, R. C., Perez-Gonzalez, V. H., Davalos, R. V., Lapizco-Encinas, B. H., *Electrophoresis* 2011, *32*, 2456–2465.

[15] Zhu, J., Hu, G., Xuan, X., *Electrophoresis* 2012, *33*, 916–922.

[16] Lewpiriyawong, N., Yang, C., Lam, Y. C., *Microfluid. Nanofluid.* 2012, *12*, 723–733.

[17] Patel, S., Showers, D., Vedantam, P., Tzeng, T. J., Qian, S., Xuan, X., *Biomicrofluid* 2012, *6*, 031402.

[18] Sabounchi, P., Huber, D. W., Kanouff, M. P., Harris, A. E., Simmons, B. A., *Twelfth International Conferences on Miniaturized Systems for Chemistry and Life Sciences*, pp. 50–52, 2008, San Diego, CA, USA.

[19] Kang, Y. J., Li, D. Q., Kalams, S. A., Eid, J. E., *Biomed. Microdev.* 2008, *10*, 243–249.

[20] Voldman, J., *Annu. Rev. Biomed. Eng.* 2006, *8*, 425–454.

[21] Xuan, X., *Electrophoresis* 2008, *29*, 33–43.

[22] Cetin, B., Li, D., *Electrophoresis* 2008, *29*, 994–1005.

[23] Ramos, A., Morgan, H., Green, N. G., Castellanos, A., *J. Phys. D* 1998, *31*, 2338–2353.

[24] Castellanos, A., Ramos, A., Gonzalez, A., Green, N. G., Morgan, H., *J. Phys. D* 2003, *36*, 2584–2597.

[25] Burg, B. R., Bianco, V., Schneider, J., Poulikakos, D., *J. Appl. Phys.* 2010, *107*, 124308.

[26] Hawkins, B. G., Kirby, B. J., *Electrophoresis* 2010, *31*, 3622–3633

[27] Sridharan, S., Zhu, J., Hu, G., Xuan, X., *Electrophoresis* 2011, *32*, 2274–2281.

[28] Zhu, J., Sridharan, S., Hu, G., Xuan, X., *J. Micromech. Microeng.* 2012, *22*, 075011.

[29] Gonzalez, A., Ramos, A., Morgan, H., Green, N. G., Castellanos, A., *J. Fluid Mech.* 2006, *564*, 415–433.

[30] Kirby, B. J., *Micro and Nano Scale Fluid Mechanics—Transport in Microfluidic Devices*, Cambridge University Press, Cambridge, UK, 2010.

[31] Morgan, H., Green, N. G., *AC Electrokinetics—Colloids and Nanoparticles*, Research Studies Press Limited, Hertfordshire, England, 2001.

[32] Venditti, R., Xuan, X., Li, D., *Microfluid. Nanofluid.* 2006, *2*, 493–399.

[33] Kirby, B. J., Hasselbrink, Jr. E. F., *Electrophoresis* 2004, *25*, 203–213.

[34] Lapizco-Encinas, B. H., Rito-Palmomares, M., *Electrophoresis* 2007, *28*, 4521–4538.

